

# Gradient based one-step fluorescence photoacoustic tomography

PRABODH KUMAR PANDEY,<sup>1</sup> OMPRAKASH GOTTAM,<sup>2</sup> NAREN NAIK,<sup>2,3,\*</sup> AND ASIMA PRADHAN<sup>1,3</sup>

<sup>1</sup>Indian Institute of Technology, Kanpur, Department of Physics, Kanpur, 208016, India

<sup>2</sup>Indian Institute of Technology, Kanpur, Department of Electrical Engineering, Kanpur, 208016, India

<sup>3</sup>Indian Institute of Technology, Kanpur, Centre for Laser and Photonics, Kanpur, 208016, India

\*[nnaik@iitk.ac.in](mailto:nnaik@iitk.ac.in)

**Abstract:** We propose a gradient based scheme to solve the fluorescence photoacoustic tomographic (FPAT) problem in a fully-nonlinear one-step setting, which aims to reconstruct the map of the absorption coefficient of an exogenous fluorophore from boundary photoacoustic pressure data. Adjoint based gradient evaluation is presented for the FPAT problem in a frequency-domain photoacoustic equation setting. Numerical validations of the resulting BFGS reconstruction scheme have been carried out in two-dimensions for full as well as limited data test-cases, and the results are compared with existing Jacobian based one-step FPAT reconstructions. The reasonably comparable results of the one-step gradient and Jacobian based FPAT reconstruction schemes coupled with the significant computational savings of the former, potentially set up the one-step gradient based schemes as an advantageous method of choice for FPAT reconstructions. Further reconstruction studies carried out using QPAT based chromophore reconstructions as inputs to the FPAT inversions, show a robustness of fluorophore absorption coefficient reconstructions to the QPAT-obtained inputs.

## 1. Introduction

Photoacoustic tomography (PAT) yields a map of the absorbed optical energy density (AOED) in a tissue medium, from measured pressure signals obtained due to a heat source formed by the interaction of incident laser radiation with the tissue of interest [1]. The obtained AOED can also be further used to reconstruct the underlying optical parameters of the medium; this tomographic optical-parameters retrieval is known in the literature as quantitative photoacoustic tomography (QPAT) [2–18].

Absorption contrast (due to intrinsic chromophore distribution) at the early stages of tumor development may not be strong enough for an accurate diagnosis [19]. In such cases, exogenous fluorescence markers are injected to tag the tumor cells and the reconstructed maps of their concentration are reconstructed in order to provide contrast enhanced images of the underlying pathology. This aspect in addition to the progress in the development of high quantum efficiency and low toxicity fluorophores [20, 21] has led to the importance of quantitative fluorescence photoacoustic tomography.

The idea of quantitative fluorescence photoacoustic tomography (FPAT),

and first such optical parameter reconstructions from assumed AOED data were demonstrated using Newton's method by Ren and Zhao in the diffusion-approximation [22]. Radiative transport equation (RTE) based algorithms were also developed in [23, 24] and reconstructions of optical parameters from AOED data were demonstrated in scattering-dominant as well as non-scattering-dominant media. The algorithms in [22, 23] involve computation of adjoint assisted Hessians and gradients at each iterate to carry out reconstructions.

A quantitative/fluorescence PAT (QPAT/FPAT) problem basically involves two steps: reconstruction of **(a)** AOED from boundary PA data, and **(b)** the desired optical parameters considering the reconstructed AOED map as internal data. The works [22–24] deal only with the second step of the FPAT problem. To address the aspect that the reconstruction errors from the first PA step cannot simply be modeled as random noise, as well as to cut-down numerical errors in two-step reconstructions, the complete nonlinear FPAT problem of reconstructing optical parameters from actually measured boundary pressure data was solved with a Jacobian based one-step inversion scheme [25, 26]. The one-step algorithm was observed to produce superior reconstruction results as compared to the two-step algorithm where the AOED was reconstructed first, followed by a second step optical parameter reconstruction. Similar results were reported for non-fluorescence QPAT as well [17, 18].

With the objective of reducing computational complexity associated with the nonlinear optimization schemes, the use of gradient-based algorithms ([2–9] for two-step, and [10–13] for one-step schemes) have been considered in place of Jacobian-based ones ([14–16] for two-step, and [17, 18] for one-step schemes) in QPAT. However, it has been previously reported in literature that the gradient based method does not give as accurate results as the Jacobian-based method both visually and quantitatively [5]. If the gradient based scheme does comparably well as the Jacobian based one for a significant class of test cases, then that is a justification of the necessity of the computationally much lighter gradient based methods. That has indeed been found in the FPAT formulation proposed by us in this paper.

In our present work, for a frequency-domain PA-equation modeled FPAT problem, adjoint-based gradients have been evaluated, and then used in a BFGS scheme to obtain reconstructions for optical absorption coefficient of exogenous fluorophore at excitation wavelength for full- as well as limited-data test cases. To the best of our knowledge, these are the first full-FPAT reconstructions with a gradient based inversion. While the existing results in FPAT consider known intrinsic absorption coefficient maps, in practice those need to be reconstructed using QPAT. We have thus also considered a phantom with unknown intrinsic absorption properties, and used QPAT to reconstruct the absorption coefficients at excitation and emission wavelengths. These reconstructed chromophore maps (instead of the actual maps) are then used in the proposed FPAT scheme to reconstruct  $\mu_{axf}$ ; the  $\mu_{axf}$  reconstructions obtained show a robustness with

respect to the QPAT-obtained inputs.

The rest of this manuscript is constructed as follows. The forward model of the coupled FPAT problem, and corresponding inverse problem are provided in section 2. The adjoint assisted gradient based scheme for one-step reconstruction is formulated in section 3. Section 4 deals with the numerical test-cases considered in the present work, and provides a detailed discussion of the reconstruction results thus obtained. The concluding remarks are offered in section 5. Appendix A briefly discusses the finite element (FE) formulation of the coupled diffusion equations (CDE) in nodal basis, and appendix B contains the corresponding adjoint equations and excitation and emission fluence sensitivities. Appendix C contains the FE formulation for solving the gradient evaluation related adjoint equations and corresponding sensitivities evaluation. The FE formulation of the CDE and the corresponding adjoint equations provided in appendices A and C are similar to [27]. However, in our calculations, the domain parameters are implemented in nodal basis while in [27] they have been implemented in elemental basis.

## 2. Problem definition

When biological markers are injected in the tissue like medium, they get tagged with the cancerous tissues and fluoresce on excitation. Recovery of the sources of fluorescent emissions i.e. the spatial concentration map or the absorption coefficient map  $\mu_{axf}(\vec{r})$  of the markers reveal the size and location of tumors inside the tissue. A fluorescent photoacoustic tomography (FPAT) problem aims to recover the map of optical parameters such as absorption and scattering coefficients of chromophores and fluorophores, anisotropy factor, etc. in the region of interest from the measured PA pressure data. In this section, we briefly introduce the forward and inverse problems of FPAT.

### 2.1. Forward Model

#### 2.1.1. Fluorescent light propagation

The fluorescence photoacoustical forward problem is the prediction of the measured pressure data assuming known optical properties of the medium, via the solution of the photoacoustic equation (PAE); in our work we use the frequency domain PAE (Helmholtz equation) [28]:

$$(\nabla^2 + k^2)p(\vec{r}, k) = ik \frac{v\beta}{C_p} h(\vec{r}) \quad (1)$$

where  $h(\vec{r}) = k_x(\vec{r})\Phi_x(\vec{r}) + k_m(\vec{r})\Phi_m(\vec{r})$  is the total absorbed optical energy density (AOED), with absorbing boundary condition (ABC) [29]:

$$\vec{n} \cdot \nabla p(\vec{r}) + ikp(\vec{r}) = 0 \quad \text{on } \partial\Omega_p \quad (2)$$

with  $\Phi_x$  (respectively  $\Phi_m$ ) being the excitation (respectively emission) fluence, and  $k_{x/m} = \mu_{a(x/m)i} + \mu_{a(x/m)f}$ , where  $\mu_{axi}$  (respectively  $\mu_{ami}$ ) is the absorption

coefficient of the intrinsic chromophore at excitation (respectively emission) wavelength; and correspondingly  $\mu_{a(x/m)f}$  being the excitation / emission absorption coefficients of the fluorophores.  $k$  is the acoustical wavenumber,  $v$  is the speed of sound,  $\beta$  is volumetric expansion coefficient,  $C_P$  is the specific heat at constant pressure.

The distribution of excitation and emission fluences in the medium is governed by the coupled diffusion equations (CDE) [27] for excitation ( $x$ ) and emission ( $m$ ) wavelengths as:

$$-\nabla \cdot (D_q \nabla \Phi_q) + k_q \Phi_q = S_q \quad (q = x, m) \quad \text{in } \Omega_d \quad (3)$$

where  $D_q = \frac{1}{3(\mu_{aqi} + \mu_{aqf} + \mu'_{sq})}$  and

$$S_q = \begin{cases} S_x, & \text{for } q = x \\ \beta \Phi_x, & \text{for } q = m \end{cases}$$

with  $\beta = \phi \mu_{axf}$ , where  $\phi$  denotes the quantum efficiency of the exogenous fluorophores. The boundary conditions are Robin boundary conditions for  $q = x, m$

$$\vec{n} \cdot (D_q \nabla \Phi_q) + b_q \Phi_q = 0 \quad \text{on } \partial \Omega_d \quad (4)$$

with  $b_q = \frac{1-R_q}{2(1+R_q)}$ ;  $R_q$  being the Fresnel reflection coefficients.

## 2.2. The measurement equation

In our work, we focus on the reconstruction of  $\mu_{axf}$ , the fluorophore absorption coefficient at excitation wavelength. The discretized heat source  $\underline{h}$  for a nominal discretized distribution of fluorophore absorption coefficient  $\underline{\mu}_{axf}$  is given by:

$$\underline{h} \equiv \mathcal{H}(\underline{\mu}_{axf}) = \sum_{q=x,m} (\underline{\mu}_{aqi} + \underline{\mu}_{aqf}) \odot \Phi_q \quad (5)$$

where  $\mathcal{H}$  denotes the heat source operator,  $\odot$  represents the pointwise multiplication and  $\Phi_{q=x,m}$  are obtained by solving (24). The forward problem of FPAT, defined in the above subsection is discretized in our work in a finite element method (FEM) framework to yield a nonlinear relation between the PA pressure data vector  $\underline{p}_{meas}$  measured at detector positions  $\vec{r}_{d_i} (i = 1, \dots, M)$  at frequencies  $\omega_j (j = 1, \dots, L)$ , and the unknown fluorophore absorption coefficient vector  $\underline{\mu}_{axf}$  in the domain, and can be written as :

$$\underline{p}_{meas} = \mathbf{J}_h \mathcal{H}(\underline{\mu}_{axf}) \equiv \mathcal{G}(\underline{\mu}_{axf}) \quad (6)$$

where the PA measurement operator  $\mathbf{J}_h$  which relates the PA measurements with the heat source  $h$ , and discrete-domain FPAT measurement operator  $\mathcal{G} = \mathbf{J}_h \mathcal{H}$  which relates the PA measurements with the fluorophore absorption coefficient  $\mu_{axf}$ , are explicitly given in [26].

### 2.3. Inverse problem

The FPAT inverse problem can be written as:

$$\hat{\underline{\mu}}_{axf} = \arg \min_{\underline{\mu}_{axf}} \epsilon(\underline{\mu}_{axf}) = \frac{1}{2} \|\underline{p}_{meas} - \mathcal{G}(\underline{\mu}_{axf})\|^2 \quad (7)$$

In general, we assume knowledge of  $\mu_{a(x/m)i}$  and  $\mu'_{s(x/m)}$  which can be obtained in principle via QPAT at excitation and emission wavelengths [17, 30] before fluorophore injection, and focus on reconstruction of  $\mu_{axf}$ .

### 3. Reconstruction scheme

The nonlinear optimization problem corresponding to one-step FPAT seeking  $\mu_{axf}$  reconstruction from boundary PA data, can be written as the minimization of the data-residual, expressed as:

$$\hat{\underline{\mu}}_{axf} = \arg \min_{\underline{\mu}_{axf}} \epsilon(\underline{\mu}_{axf}) = \frac{1}{2} \|\underline{p}_{meas} - \mathcal{G}(\underline{\mu}_{axf})\|^2 \quad (8)$$

#### 3.1. Gradient computation

The first variation of the above functional can be written (using Eq. (5),(6)) as:

$$\begin{aligned} \delta \epsilon(\underline{\mu}_{axf}) &= -(\underline{p}_{meas} - \mathcal{G}(\underline{\mu}_{axf}))^T \delta(\mathcal{G}(\underline{\mu}_{axf})) \\ &= -(\underline{p}_{meas} - \mathcal{G}(\underline{\mu}_{axf}))^T \mathbf{J}_h \delta \mathcal{H}(\underline{\mu}_{axf}) \\ &= -\underline{v}^T \delta \mathcal{H}(\underline{\mu}_{axf}) = -(\delta \mathcal{H}(\underline{\mu}_{axf}))^T \underline{v} \\ &= -\left( \underline{k}_x \odot \delta \underline{\phi}_x + \underline{\phi}_x \odot \delta \underline{k}_x + \underline{k}_m \odot \delta \underline{\phi}_m + \underline{\phi}_m \odot \delta \underline{k}_m \right)^T \underline{v} \end{aligned} \quad (9)$$

where  $\underline{v} := \mathbf{J}_h^T(\underline{p}_{meas} - \mathcal{G}(\underline{\mu}_{axf}))$ . Also since  $\underline{k}_x = \underline{\mu}_{axi} + \underline{\mu}_{axf}$ ,  $\implies \delta \underline{k}_x = \delta \underline{\mu}_{axf}$  and  $\underline{k}_m = \underline{\mu}_{ami} + \gamma \underline{\mu}_{axf}$   $\implies \delta \underline{k}_m = \gamma \delta \underline{\mu}_{axf}$  ( $\gamma$  being the ratio of the absorption coefficients of exogenous fluorophore, at the emission and excitation wavelengths:  $\gamma = \frac{\mu_{amf}}{\mu_{axf}}$ ), we obtain,

$$\begin{aligned} \delta \epsilon &= -\left( \underline{k}_x \odot \delta \underline{\phi}_x + \underline{\phi}_x \odot \delta \underline{\mu}_{axf} + \underline{k}_m \odot \delta \underline{\phi}_m + \gamma \underline{\phi}_m \odot \delta \underline{\mu}_{axf} \right)^T \underline{v} \\ &\equiv \delta \epsilon_1 + \delta \epsilon_2 + \delta \epsilon_3 + \delta \epsilon_4 \end{aligned} \quad (10)$$

The second and fourth terms ( $\delta \epsilon_2$  and  $\delta \epsilon_4$  respectively of Eq. (10)) can be written as:

$$\delta \epsilon_2 = -(\underline{\phi}_x \odot \delta \underline{\mu}_{axf})^T \underline{v} = (\delta \underline{\mu}_{axf})^T (-\underline{v} \odot \underline{\phi}_x) \quad (11)$$

and

$$\delta \epsilon_4 = (\underline{\phi}_m \odot \delta \underline{\mu}_{axf})^T (-\gamma \underline{v}) = (\delta \underline{\mu}_{axf})^T (-\gamma \underline{v} \odot \underline{\phi}_m) \quad (12)$$

The first term of Eq. (10)

$$\delta\epsilon_1 = -\underline{v}^T(\underline{k}_x \odot \delta\phi_x) = -\sum_{w=1}^N v_w k_{xw} \delta\Phi_x^{(w)} \quad (13)$$

where  $w$  denotes the nodes in the domain. The relation between  $\delta\Phi_x$  and adjoint  $\psi_{xx}$  is linear (Eq. (37) in Appendix C), and can be written in the form,

$$\delta\Phi_x^{(w)} = \mathcal{L}_{xx}(\psi_{xx}^{(w)})\delta\mu_{axf} \quad (14)$$

where  $\psi_{xx}^{(w)}$  is the solution to the adjoint problem with Dirac source at the  $w^{th}$  node ( $\underline{\Delta}^{(w)}$ ):  $\mathbf{A}_x \psi_{xx}^{(w)} = \underline{\Delta}^{(w)}$ , and  $\mathcal{L}_{xx}$  is defined in Eq. (37) (in Appendix C). Therefore,

$$\begin{aligned} \delta\epsilon_1 &= -\sum_{w=1}^N v_w k_{xw} \mathcal{L}_{xx}(\psi_{xx}^{(w)})\delta\mu_{axf} = -\mathcal{L}_{xx}\left(\sum_{w=1}^N v_w k_{xw} \psi_{xx}^{(w)}\right)\delta\mu_{axf} \\ &= -\mathcal{L}_{xx}(\mathbf{A}_x^{-1} \sum_{w=1}^N v_w k_{xw} \underline{\Delta}^{(w)})\delta\mu_{axf} = \mathcal{L}_{xx}(\Psi_{xx})\delta\mu_{axf} = (\delta\mu_{axf})^T \underline{g}_x \end{aligned} \quad (15)$$

with  $\underline{g}_x = [\mathcal{L}_{xx}(\Psi_{xx})]^T$ , and adjoint  $\Psi_{xx}$  is solution to,

$$\mathbf{A}_x \Psi_{xx} = \underline{S}_x \quad (16)$$

where  $\underline{S}_x = -\sum_{w=1}^N v_w k_{xw} \underline{\Delta}^{(w)}$ . Similarly, using Eqs. (36) and (38), the third term of Eq. (10) can be written as:

$$\begin{aligned} \delta\epsilon_3 &= -\sum_{w=1}^N v_w k_{m_w} [\mathcal{L}_{mm}(\psi_{mm}^{(w)}) + \mathcal{L}_{xm}(\psi_{xm}^{(w)})]\delta\mu_{axf} \\ &= [-\mathcal{L}_{mm}\left(\sum_{w=1}^N v_w k_{m_w} \psi_{mm}^{(w)}\right) - \mathcal{L}_{xm}\left(\sum_{w=1}^N v_w k_{m_w} \psi_{xm}^{(w)}\right)]\delta\mu_{axf} \\ &= [-\mathcal{L}_{mm}(\mathbf{A}_m^{-1} \sum_{w=1}^N v_w k_{m_w} \underline{\Delta}^{(w)}) - \mathcal{L}_{xm}(\mathbf{A}_x^{-1} \mathbf{M}_\beta \sum_{w=1}^N v_w k_{m_w} \psi_{mm}^{(w)})]\delta\mu_{axf} \\ &= [-\mathcal{L}_{mm}(\mathbf{A}_m^{-1} \sum_{w=1}^N v_w k_{m_w} \underline{\Delta}^{(w)}) - \mathcal{L}_{xm}(\mathbf{A}_x^{-1} \mathbf{M}_\beta \mathbf{A}_m^{-1} \sum_{w=1}^N v_w k_{m_w} \underline{\Delta}^{(w)})]\delta\mu_{axf} \\ &= [\mathcal{L}_{mm}(\Psi_{mm}) + \mathcal{L}_{xm}(\Psi_{xm})]\delta\mu_{axf} = (\delta\mu_{axf})^T \underline{g}_m \end{aligned} \quad (17)$$

with  $\underline{g}_m = [\mathcal{L}_{mm}(\Psi_{mm}) + \mathcal{L}_{xm}(\Psi_{xm})]^T$ , and adjoints  $\Psi_{mm}$ ,  $\Psi_{xm}$  are solutions of,

$$\mathbf{A}_m \Psi_{mm} = \underline{S}_m, \quad \mathbf{A}_x \Psi_{xm} = \mathbf{M}_\beta \Psi_{mm} \quad (18)$$

with  $\underline{S}_m = -\sum_{w=1}^N v_w k_{mw} \underline{\Delta}^{(w)}$ . Therefore, using Eq. (11),(12),(15),(17) in Eq. (10), we can write:

$$\delta\epsilon = (\delta\mu_{\text{axf}})^T (\underline{g}_x - \underline{v} \odot \underline{\phi}_x + \underline{g}_m - \gamma \underline{v} \odot \underline{\phi}_m) \equiv (\delta\mu_{\text{axf}})^T \underline{g} \quad (19)$$

where the gradient  $\underline{g}$  is given as:

$$\underline{g} = [\mathcal{L}_{xx}(\Psi_{xx})]^T - \underline{v} \odot \underline{\phi}_x + [\mathcal{L}_{mm}(\Psi_{mm}) + \mathcal{L}_{xm}(\Psi_{xm})]^T - \gamma \underline{v} \odot \underline{\phi}_m \quad (20)$$

### 3.2. Inversion scheme

The gradient based reconstructions were carried out using BFGS algorithm [31], a quasi-Newton approach. The update direction  $\Delta\mu_{\text{axf}}^j$  at any (say  $j^{\text{th}}$ ) iterate is computed by solving,

$$\mathbf{B}^{(j)} \underline{\mu}_{\text{axf}}^{(j)} = \underline{g}^{(j)} \quad (21)$$

where  $\underline{g}^{(j)}$  is the gradient vector at present iterate, and  $\mathbf{B}^{(j)}$  is an approximation to the Hessian matrix, which is initialized as identity matrix (of size  $N \times N$ ) and updated at each iterate using

$$\mathbf{B}^{(j+1)} = \mathbf{B}^{(j)} + \frac{\underline{y}^{(j)} \underline{y}^{(j)T}}{\underline{y}^{(j)T} \underline{s}^{(j)}} - \frac{\mathbf{B}^{(j)} \underline{s}^{(j)} \underline{s}^{(j)T} \mathbf{B}^{(j)T}}{\underline{s}^{(j)T} \mathbf{B}^{(j)} \underline{s}^{(j)}} \quad (22)$$

Here  $\underline{y}^{(j)} = \underline{g}^{(j+1)} - \underline{g}^{(j)}$ , and  $\underline{s}^{(j)} = \alpha \Delta\mu_{\text{axf}}^{(j)}$  is the total update, where the steplength  $\alpha$  is computed using a line search algorithm [32].

## 4. Numerical Studies

### 4.1. Test cases

We consider the domain of interest to be of dimension  $2\text{cm} \times 2\text{cm}$ , with the overall computational domain set at  $3\text{cm} \times 3\text{cm}$  for PA modeling. The CDE (Eq. (3)) is solved in  $2\text{cm} \times 2\text{cm}$  domain to obtain the heat source, followed by solving the frequency-domain PAE (Eq. (1)) in the overall  $3\text{cm} \times 3\text{cm}$  domain. The set-ups considered in our numerical studies are depicted in Fig. 1.

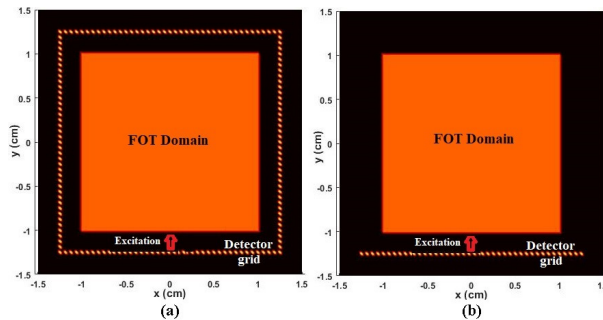


Fig. 1: Set up for computational experiments in (a) full and (b) limited data setting

**Setting-1:** Background optical properties of the CDE domain are considered to be homogeneous, with  $\mu_{axi} = 0.023\text{cm}^{-1}$ ,  $\mu_{ami} = 1.2565 \cdot \mu_{axi}$ ,  $\mu'_{sx} = 9.84\text{cm}^{-1}$ ,

---

**Algorithm 1** One-step, gradient based FPAT algorithm
 

---

```

1: procedure ONE STEP, GRADIENT BASED FPAT RECONSTRUCTION
2:    $\underline{\mu}_{axf} = \text{zeroes}(N \times 1)$  (Initialization by zero)
3:   Predict absorbed optical energy density  $\underline{h}^s$ 
4:   Compute PAT measurement matrix  $\mathbf{J}_h$ 
5:   Predict boundary PA data  $\underline{p}^s$ 
6:    $\mathbf{B} = \text{eye}(N \times N)$  (Initialization by identity)
7:    $\underline{g}_0 = \text{zeros}(N \times 1)$  (Initialization by zero)
8:   Compute  $\epsilon \leftarrow \|\underline{p}^o - \underline{p}^s\|_2^2$ 
9:   while  $\epsilon \leq \text{tol}$  or the residual is unchanging do
10:    Compute gradient  $\underline{g}$ 
11:    Compute the update direction  $\Delta \underline{\mu}_{axf}$ 
12:    Compute steplength  $\alpha$  using line search
13:    update  $\underline{s} \leftarrow \alpha \Delta \underline{\mu}_{axf}$ 
14:     $\underline{\mu}_{axf} \leftarrow \underline{\mu}_{axf} + \underline{s}$ 
15:    Predict absorbed optical energy density  $\underline{h}^s$ 
16:    Predict boundary PA data  $\underline{p}^s$ 
17:     $\underline{y} = \underline{g} - \underline{g}_0$ 
18:     $\underline{g}_0 \leftarrow \underline{g}$ 
19:     $\mathbf{B} \leftarrow \mathbf{B} + \frac{\underline{y}\underline{y}^T}{\underline{y}^T \underline{s}} - \frac{\mathbf{B} \underline{s} \underline{s}^T \mathbf{B}^T}{\underline{s}^T \mathbf{B} \underline{s}}$ 
20:    Compute  $\epsilon \leftarrow \|\underline{p}^o - \underline{p}^s\|_2^2$ 
21:  end while
22:  return  $\mu_{axf}$ 
23: end procedure

```

---

$\mu'_{sm} = \mu'_{sx}$ ,  $\Phi = 0.4$ ,  $R_{x,m} = 0.431$ ,  $\mu_{axf} = 0.005 \text{ cm}^{-1}$  and  $\mu_{amf} = 0.1012 \cdot \mu_{axf}$  [26, 33, 34]. The phantoms we aim to reconstruct are: (i) **phantom 1**: a circular fluorescent inhomogeneity ( $\mu_{axf} = 0.05 \text{ cm}^{-1}$ ) (Fig. 2a) and (ii) **phantom 2**: a concave ( $\mu_{axf} = 0.04 \text{ cm}^{-1}$ ) as well as a circular inhomogeneity ( $\mu_{axf} = 0.05 \text{ cm}^{-1}$ ) (Fig. 2b).

**Setting-2:** We have also considered a more realistic scenario, where the chromophore absorption coefficients' ( $\mu_{axi}$  and  $\mu_{ami}$ ) maps (at excitation and emission wavelengths respectively) are unknown, and reconstructed by carrying out QPAT at the two wavelengths. These reconstructed maps are then utilized to further reconstruct  $\mu_{axf}$ .

To carry out this study, we have considered a **phantom 3** with the fluorescence distribution and the background chromophore optical properties kept the same as phantom-2. It has a circular ( $\mu_{axi} = 0.04 \text{ cm}^{-1}$ ) and a concave ( $\mu_{axi} = 0.03 \text{ cm}^{-1}$ ) shaped chromophore absorption inhomogeneities with low target-background contrast ( $\sim 1.5 : 1$ ) representing early stages of tumor growth. As previously mentioned, the chromophore absorption coefficient at emission wavelength ( $\mu_{ami}$ ) is related to the absorption coefficient at excitation wavelength ( $\mu_{axi}$ ) as:  $\mu_{ami} = 1.2565 \cdot \mu_{axi}$ . The properties and distribution of the exogenous fluorophore have been kept the same as phantom-2.



The acoustic properties of the PAE modeling domain are chosen to be homogeneous:  $\beta = 4 \times 10^{-4} K^{-1}$  and  $C_P = 4000 JKg^{-1} K^{-1}$  [1, 26]. Equations

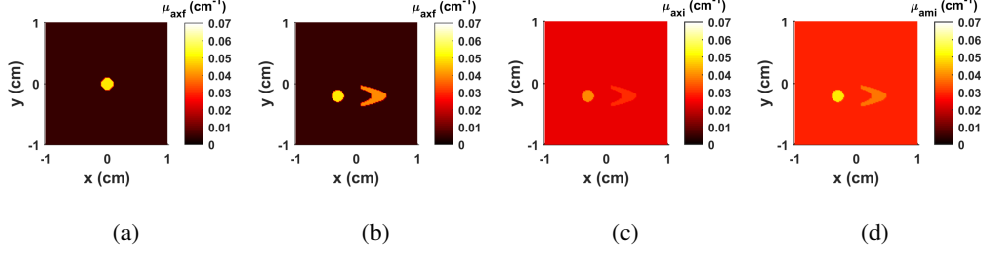


Fig. 2: True maps of  $\mu_{axf}$  (a) phantom 1, (b) phantom 2, and true (c)  $\mu_{axi}$  and (d)  $\mu_{ami}$  maps for phantom 3, which has the same  $\mu_{axf}$  map as phantom 2.

involved in this work have been solved using the finite element method. The PA data are computed at 100 frequencies between 9.6kHz to 960kHz, at 160 and 41 detector locations for full and limited data cases respectively, with detector separation of  $1/16$  cm. The experimental PA measurements are simulated at a mesh resolution of  $1/128$  cm. The gradient and forward solver computations, as well as reconstructions are carried out at  $1/64$ cm resolution.

#### 4.2. Reconstruction studies

Reconstruction procedure starts with an initial guess for  $\underline{\mu}_{axf}$  which we choose to be a zero vector. Algorithm 1 is implemented to obtain the  $\mu_{axf}$  reconstructions of phantom 1 and 2 in full and limited-data settings, displayed in Fig. 3 and 4 respectively.

Accuracy of the reconstructions has been quantified on the basis of the *correlation coefficient* ( $\rho$ ) and the *deviation factor* ( $\delta$ ) defined as [35]:

$$\rho = \frac{\sum_{i=1}^N (p_i^r - \bar{p}^r)(p_i^t - \bar{p}^t)}{(N-1)\Delta p^r \Delta p^t}; \quad \delta = \frac{\sqrt{\sum_{i=1}^N (p_i^r - p_i^t)^2 / N}}{\Delta p^t} \quad (23)$$

where  $N$  is the total number of nodes,  $\Delta p^t$  and  $\Delta p^r$  are the standard deviations and  $\bar{p}^t$  and  $\bar{p}^r$  are the mean values of the true and reconstructed values of the parameter respectively. The error measures ( $\rho, \delta$ ) obtained for these reconstructions are tabulated in (Table 1), alongside those obtained from Jacobian based reconstructions [26].

It is observed that, when PA data is noiseless, accurate reconstructions are obtained for both the phantoms using the gradient based scheme in full data settings (Fig. 3(a,e)). With increasing noise level in measurements, the reconstructions display noisy artifacts. However, the shape of inhomogeneities and parameter values are accurately reconstructed for noisy data (even with SNR as low as 5dB) as well, as displayed in figure 3.

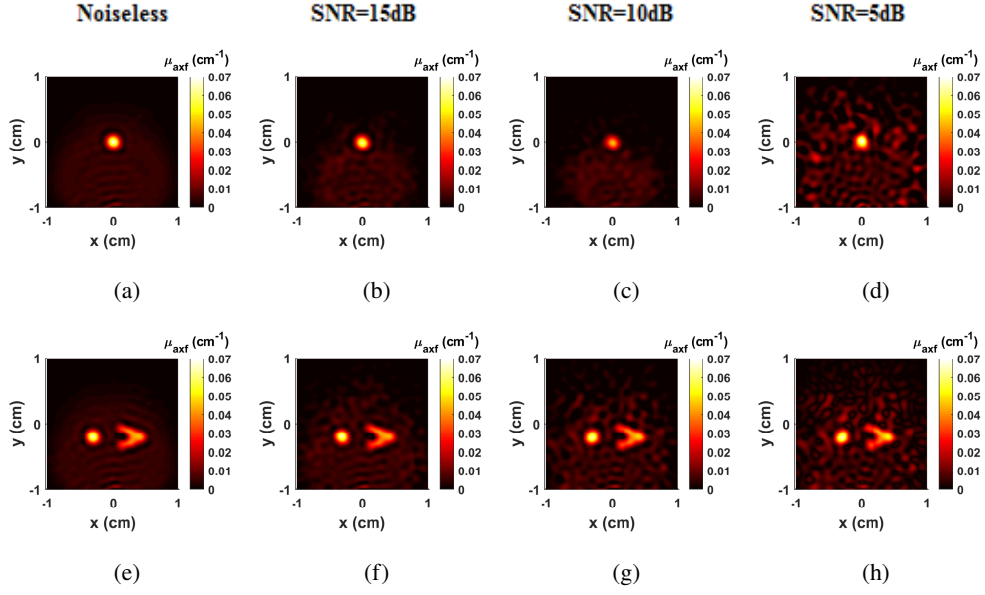


Fig. 3: Reconstruction results obtained for full-data setting for (a,e) noiseless PA data, and data with (b,f) 15dB , (c,g) 10dB, and (d,h) 5dB SNR

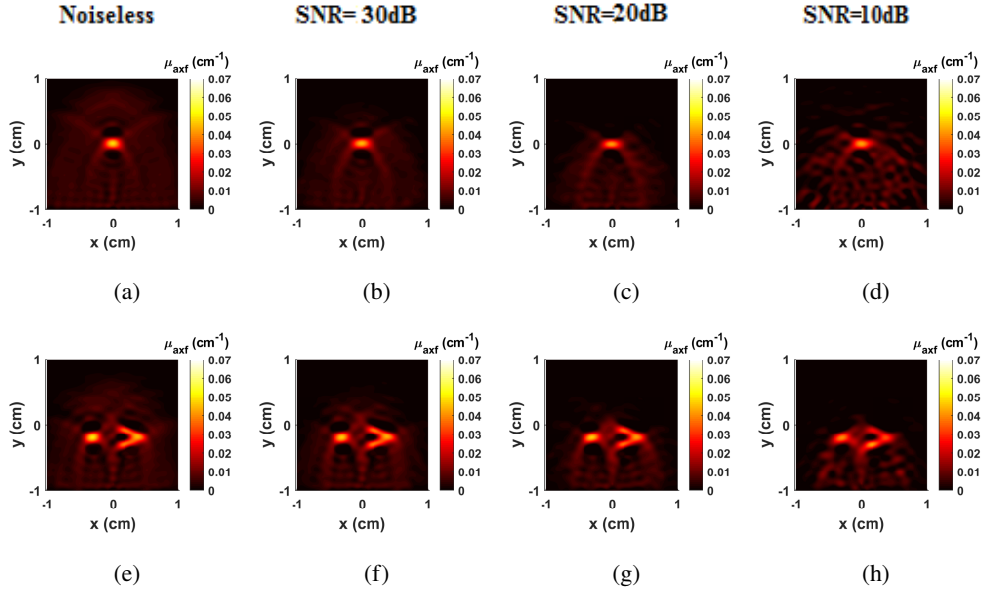


Fig. 4: Reconstruction results obtained for limited-data setting for (a,e) noiseless PA data, and data with (b,f) 30dB , (c,g) 20dB, and (d,h) 10dB SNR

Table 1: Correlation coefficients  $\rho$  and deviation factors  $\delta$  for one-step Jacobian and gradient based reconstructions

Data setting	Phantom	SNR	Jacobian based		Gradient based	
			$\rho$	$\delta$	$\rho$	$\delta$
Full data	Phantom-1	Noiseless	0.82	0.74	0.81	0.89
		15dB	0.78	0.87	0.78	1.02
		10dB	0.74	0.90	0.67	1.13
		5dB	0.67	0.97	0.63	1.13
	Phantom-2	Noiseless	0.87	0.57	0.85	0.65
		15dB	0.85	0.63	0.84	0.67
		10dB	0.81	0.68	0.82	0.70
		5dB	0.77	0.74	0.74	0.91
Limited data	Phantom-1	Noiseless	0.80	0.63	0.70	0.79
		30dB	0.70	0.78	0.63	1.03
		20dB	0.57	1.02	0.59	1.17
		10dB	0.49	1.18	0.56	1.13
	Phantom-2	Noiseless	0.85	0.54	0.79	0.69
		30dB	0.82	0.61	0.77	0.77
		20dB	0.75	0.74	0.75	0.85
		10dB	0.71	0.87	0.69	0.94

Under limited data settings, the reconstructions carry characteristic directional artifacts. Using the proposed scheme, the reconstructions with noisy data are found to reconstruct the inhomogeneities accurately. However, at low SNRs, though inhomogeneities are located well, the reconstructed parameter values are not that accurate. Artifacts in the reconstructions are more prominent as compared to those observed under full data settings.

The reconstructions obtained from the proposed gradient based scheme were further compared with the results obtained using a Jacobian based scheme [26], and tabulated in table 1. In full data settings, the gradient based scheme yields similar results as obtained from the Jacobian based reconstructions for  $SNR > 10dB$ . However, the artifacts in the gradient based reconstructions are more than they are in the Jacobian based reconstructions for low SNR. In the limited data test cases, the BFGS scheme yields relatively lower correlation coefficients and higher deviation factors as compared to the Jacobian based scheme.

It needs to be noted though, that computation of Jacobian at each iterate requires solving the corresponding adjoint models (to obtain  $\{\psi_{xx}, \psi_{mm}, \psi_{xm}\}$ )  $N$  (number of nodes in the domain) times. While, computation of gradient requires these models (to obtain  $\{\Psi_{xx}, \Psi_{mm}, \Psi_{xm}\}$ ) to be solved only once. In FPAT, for the settings presented in this manuscript, the Jacobian computation needs  $3 \times 16641$  runs (for 3 adjoints and 16641 nodes in the domain), while the proposed gradient computation requires 3 runs of the corresponding adjoint solvers. Therefore, even

though gradient based scheme is observed to need higher number of iterations for convergence, it produces reconstructions significantly faster than the Jacobian based scheme. The computational advantage of the gradient based scheme with respect to Jacobian based scheme naturally improves with increase in the number of nodes in the reconstruction domain, thus making it a powerful method of choice in three-dimensions or dynamic settings.

The existing FPAT results in literature demonstrate reconstructions for known and homogeneous chromophore distribution, and the reconstruction studies for phantom 1 and 2 (Fig 3 and 4) have also been carried out under the same assumptions. In case of phantom 3, we have considered a more realistic problem, where the chromophore absorption coefficients' ( $\mu_{axi}$  and  $\mu_{ami}$ ) maps (at excitation and emission wavelengths respectively) are first reconstructed by carrying out QPAT at the two wavelengths and then utilized to further reconstruct  $\mu_{axf}$  using the FPAT scheme proposed in this paper.

The  $\mu_{a(x/m)i}$  maps were reconstructed using a one-step Jacobian based QPAT scheme as in [17] with the initial guess for the  $\mu_{a(x/m)i}$  being  $0.01 \text{ cm}^{-1}$  distributed uniformly in the domain. The reconstructed  $\mu_{a(x/m)i}$  maps were then utilized to reconstruct  $\mu_{axf}$  using Algorithm 1 proposed in section 3. The reconstruction results thus obtained for full and limited data settings are provided in Fig. 5 and corresponding error measures are provided in Table 2.

Table 2: Correlation coefficients  $\rho$  and deviation factors  $\delta$  for  $\mu_{axf}$  reconstructions, when  $\mu_{a(x/m)i}$  were reconstructed using QPAT

Data setting	SNR	$\mu_{axf}$	
		$\rho$	$\delta$
Full data	Noiseless	0.85	0.53
	10dB	0.77	0.74
Limited data	Noiseless	0.75	0.75
	20dB	0.72	0.90

Early stages of tumor are associated with low absorption contrast [19]. As evident in Fig. 5, the QPAT reconstructions of  $\mu_{a(x/m)i}$  result in poor contrast, and the shapes and sizes of the tumors cannot be retrieved precisely especially under noisy and limited data settings. Exogenous fluorescent markers are injected in the tissue which tag the tumors and reconstruction of their distribution yields contrast enhanced images as illustrated in  $\mu_{axf}$  reconstructions carried out using Algorithm 1 depicted in Fig. 5(c,f,i,l). It is observed that the fluorescence targets have been reconstructed quite well for noiseless as well as noisy PA data in both full and limited data settings. Also, under noisy and limited data settings while the  $\mu_{a(x/m)i}$  reconstructions carry artifacts, we are still able to reconstruct the  $\mu_{axf}$  reasonably well. Therefore the FPAT reconstructions are seen to be robust

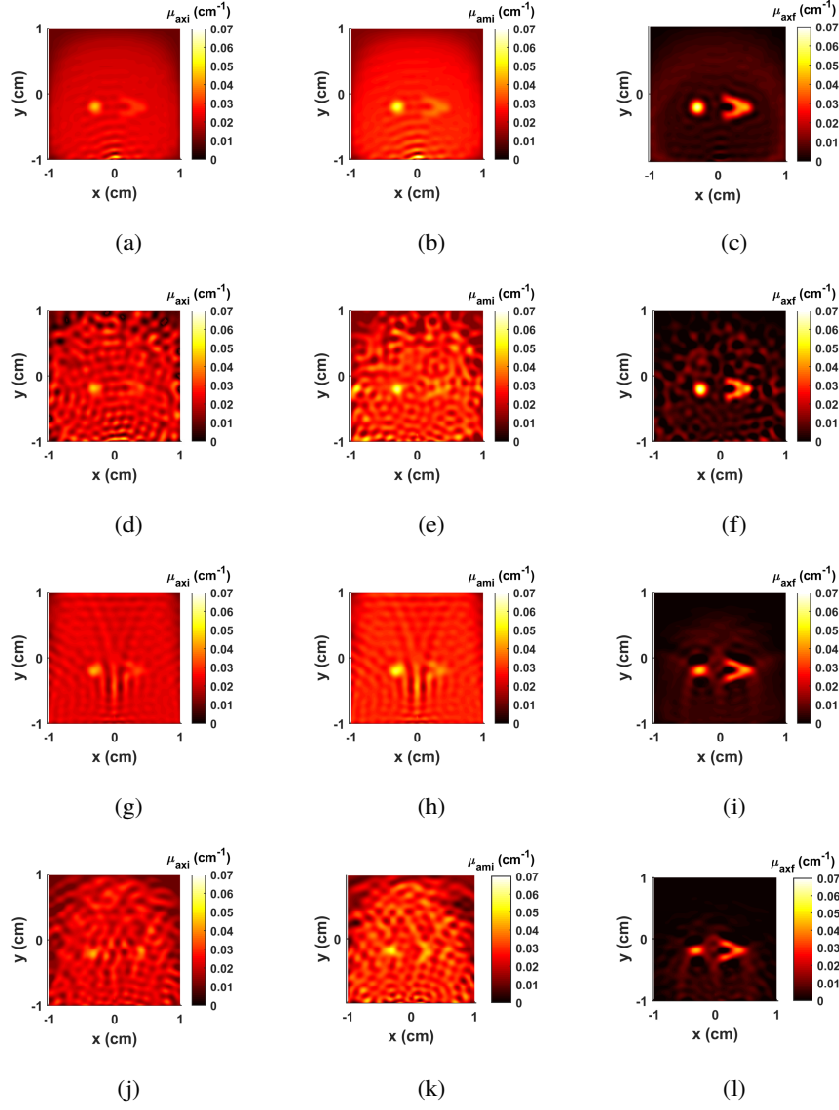


Fig. 5: The first two rows correspond to the (noiseless and 10dB SNR respectively) full data reconstructions, while the bottom two rows display the (noiseless and 20dB SNR respectively) limited data reconstructions. The first column (a,d,g,j) corresponds to  $\mu_{axi}$  reconstructions, the second column (b,e,h,k) corresponds to  $\mu_{ami}$  reconstructions, and third column (c,f,i,l) corresponds to  $\mu_{axf}$  reconstructions.

with respect to the QPAT reconstruction errors.

## 5. Conclusion

A gradient based BFGS reconstruction scheme for one-step FPAT has been developed, to reconstruct the fluorophore absorption coefficient at excitation wavelength from boundary PA (pressure) data in a frequency-domain PA-equation-modeled setting. An adjoint based scheme has been developed for gradient computation. The gradients evaluated were implemented in a BFGS scheme to obtain reconstructions under full as well as limited data settings. To the best of our knowledge, these are the first results on gradient based one-step FPAT reconstructions.

The results thus obtained were compared with existing Jacobian based reconstructions [26]. Over the test cases considered here, the gradient and Jacobian based schemes perform comparably for PA measurements obtained in full data setting. The Jacobian based scheme yields slightly better reconstructions as compared to the gradient based schemes under very noisy as well as limited data settings, but at a much higher computational cost.

Construction of Jacobian needs the adjoint model to be solved  $O(N)$  ( $N$ : number of nodes in the domain) times while for computation of gradient, it needs to be solved  $O(1)$  times. Therefore, although the gradient based scheme took larger number of iterations to converge, overall it was found to be significantly faster as compared to the Jacobian based scheme. The reasonably comparable results of the gradient and Jacobian based reconstruction schemes coupled with the significant computational savings of the former, potentially set up the one-step gradient based schemes as an advantageous method of choice for FPAT reconstructions with good scale up possibilities to 3D and dynamic settings.

Reconstruction studies have also been performed to study the sensitivity of FPAT reconstructions with respect to the QPAT reconstruction errors. A phantom with low-contrast absorption inhomogeneities was considered and the QPAT at excitation and emission wavelengths were carried out to reconstruct the absorption coefficient maps at excitation and emission wavelengths ( $\mu_{a(x/m)i}$ ). These reconstructions were utilized in the proposed FPAT scheme to reconstruct the  $\mu_{axf}$  (fluorophore absorption coefficient at excitation wavelength) map. It is observed that the fluorescence targets thus obtained have been reconstructed quite well for noiseless as well as noisy PA data in both full and limited data settings. The  $\mu_{axf}$  reconstructions were found to be reasonably good even when QPAT reconstructions carried artifacts, especially in the cases with noisy PA measurements and limited data settings, indicating the robustness of the proposed scheme.

## Disclosures

The authors declare no conflicts of interest.

*Acknowledgements:* PKP acknowledges the support of CSIR and BRNS India during parts of the work.

### Appendix A: Finite element formulation of coupled diffusion equations

The FE formulation of the CDE and the corresponding adjoint equations provided in appendices A and C are similar to [27]. However, in our calculations, the domain parameters are implemented in nodal basis while in [27] they have been implemented in elemental basis. Using Galerkin's formulation and expressing the variables in finite element nodal basis, the CDE can be expressed in a discretized form as (similar to Eq.(31) of [27]):

$$\mathbf{A}_q \Phi_q = \underline{s}_q; \quad q = x \text{ or } m \quad (24)$$

where subscripts  $q = x \text{ or } m$  imply the quantities at excitation and emission wavelengths. The domain parameters  $C \in \{D_q, k_q, b_q, \beta\}$  are implemented in nodal basis. System matrices  $\mathbf{A}_q$  (or  $\mathbf{A}(D_q, k_q, b_q)$ ) and  $\mathbf{M}_\beta$  (or  $\mathbf{M}(\beta)$ ) are the assembled form of elemental matrices  $\mathcal{A}_q(D_q, k_q, b_q)$  and  $\mathcal{M}(\beta)$  respectively, defined as (similar to Eq.(38),(39) of [27])

$$\mathcal{A}_q(D_q, k_q, b_q) = \mathcal{K}_1 D_q + \mathcal{K}_2 k_q + \mathcal{K}_3 b_q; \quad \mathcal{M}(\beta) = \mathcal{K}_2 \beta. \quad (25)$$

where,

$$\begin{aligned} \mathcal{K}_1 D_q &= \left[ \sum_{j=1}^3 \int_{\Omega_e} N_j D_{qj} (\nabla[\mathbf{N}])^T \nabla[\mathbf{N}] \right] = \int_{\Omega_e} (\nabla[\mathbf{N}])^T [\mathbf{N}] \tilde{D}_q \nabla[\mathbf{N}], \\ \mathcal{K}_2 k_q &= \left[ \sum_{j=1}^3 \int_{\Omega_e} N_j k_{qj} [\mathbf{N}]^T [\mathbf{N}] \right] = \int_{\Omega_e} [\mathbf{N}]^T [\mathbf{N}] \tilde{k}_q [\mathbf{N}], \\ \mathcal{K}_2 \beta &= \left[ \sum_{j=1}^3 \int_{\Omega_e} N_j \beta_j [\mathbf{N}]^T [\mathbf{N}] \right] = \int_{\Omega_e} ([\mathbf{N}])^T [\mathbf{N}] \tilde{\beta} [\mathbf{N}], \\ \mathcal{K}_3 b_q &= \left[ \sum_{j=1}^3 \int_{\partial\Omega_e} N_j b_{qj} [\mathbf{N}]^T [\mathbf{N}] \right] = \int_{\partial\Omega_e} (\nabla[\mathbf{N}])^T [\mathbf{N}] \tilde{b}_q \nabla[\mathbf{N}] \end{aligned} \quad (26)$$

$[\mathbf{N}] = [N_1 \ N_2 \ N_3]$  being the linear basis function (size:  $1 \times 3$ ) for a triangular element  $e$ , and  $\nabla[\mathbf{N}]$  denotes its gradient matrix (size:  $2 \times 3$ ). Index  $j$  ( $= 1, 2, 3$ ) corresponds to the nodes in element  $e$ .  $\mathcal{K}_i$ ,  $i = 1, 2, 3$  denote that integral matrix operators for a nodal basis representation of the parameters. The parameters  $C \in \{D_{qj}, k_{qj}, b_{qj}, \beta_j\}$  are represented in nodal basis, i.e. the value of coefficient  $C$  at any point in an element can be expressed as  $C = \sum_{j=0}^3 N_j C_j = [\mathbf{N}] \tilde{C}$ , where  $\tilde{C} = [C_1 \ C_2 \ C_3]^T$  (size:  $3 \times 1$ ) denotes the nodal values of parameter  $C$  in element  $e$ . The source vectors are defined as,

$$\underline{s}_q = \begin{cases} \underline{s}_x, & \text{for } q = x \\ \mathbf{M}_\beta \Phi_x, & \text{for } q = m \end{cases}$$

where  $\underline{s}_x$  is the assembled form of  $S_x = Q[N_1(\vec{r}_s) \ N_3(\vec{r}_s) \ N_3(\vec{r}_s)]^T$ ;  $Q$  and  $\vec{r}_s$  being the strength and location of the point source.

The discretized heat source for a nominal distribution of fluorophore absorption coefficient  $\underline{\mu}_{axf}$  is given by:

$$\underline{h} \equiv \mathcal{H}(\underline{\mu}_{axf}) = \sum_{q=x,m} (\underline{\mu}_{aqi} + \underline{\mu}_{aqf}) \odot \underline{\Phi}_q \quad (27)$$

where  $\mathcal{H}$  denotes the heat source operator,  $\odot$  represents the pointwise multiplication and  $\underline{\Phi}_{q=x,m}$  are obtained by solving (24).

### Appendix B: Adjoint based fluence sensitivities [27]

The sensitivity calculations are the same as Eq.(21)-(26) of [27] and are provided here for completeness and clarity of the notations.

If the adjoints  $\psi_{xx}$ ,  $\psi_{mm}$ ,  $\psi_{xm}$  satisfy:

$$-\nabla \cdot (D_x \nabla \psi_{xx}) + k_x \psi_{xx} = \Delta_d \quad \text{on } \Omega \quad (28)$$

$$\vec{n} \cdot (D_x \nabla \psi_{xx}) + b_x \psi_{xx} = 0 \quad \text{on } \partial\Omega \quad (29)$$

$$-\nabla \cdot (D_m \nabla \psi_{mm}) + k_m \psi_{mm} = \Delta_d \quad \text{on } \Omega \quad (30)$$

$$\vec{n} \cdot (D_m \nabla \psi_{mm}) + b_m \psi_{mm} = 0 \quad \text{on } \partial\Omega \quad (31)$$

$$-\nabla \cdot (D_x \nabla \psi_{xm}) + k_x \psi_{xm} = \beta \psi_{mm} \quad \text{on } \Omega \quad (32)$$

$$\vec{n} \cdot (D_x \nabla \psi_{xm}) + b_x \psi_{xm} = 0 \quad \text{on } \partial\Omega \quad (33)$$

the perturbed excitation and emission fluence can be expressed as:

$$\delta\Phi_x = - \int_{\Omega} \nabla \psi_{xx} \frac{\partial D_x}{\partial p} \delta p \nabla \Phi_x - \int_{\Omega} \psi_{xx} \frac{\partial k_x}{\partial p} \delta p \Phi_x - \int_{\Omega} \psi_{xx} \frac{\partial b_x}{\partial p} \delta p \Phi_x \quad (34)$$

$$\begin{aligned} \delta\Phi_m = & - \int_{\Omega} \nabla \psi_{mm} \frac{\partial D_m}{\partial p} \delta p \nabla \Phi_m - \int_{\Omega} \psi_{mm} \frac{\partial k_m}{\partial p} \delta p \Phi_m - \int_{\Omega} \psi_{mm} \frac{\partial b_m}{\partial p} \delta p \Phi_m \\ & - \int_{\Omega} \nabla \psi_{xm} \frac{\partial D_x}{\partial p} \delta p \nabla \Phi_x - \int_{\Omega} \psi_{xm} \frac{\partial k_x}{\partial p} \delta p \Phi_x - \int_{\Omega} \psi_{xm} \frac{\partial b_x}{\partial p} \delta p \Phi_x + \int_{\Omega} \psi_{mm} \frac{\partial \beta}{\partial p} \delta p \Phi_x \end{aligned} \quad (35)$$

### Appendix C: Finite element formulation of Adjoint and fluence sensitivities

Solving for the adjoints (Eq. (28)-(33)) using Galerkin's formulation yields (similar to Eq.(42)-(44) of [27])

$$\mathbf{A}_x \underline{\psi}_{xx}^{(w)} = \underline{\Delta}^{(w)}; \quad \mathbf{A}_m \underline{\psi}_{mm}^{(w)} = \underline{\Delta}^{(w)}; \quad \mathbf{A}_x \underline{\psi}_{xm}^{(w)} = \mathbf{M}_{\beta} \underline{\psi}_{mm}^{(w)} \quad (36)$$

where  $\underline{\Delta}^{(w)}$  denotes the source vector corresponding to a point source with unit strength at  $w^{th}$  node. Using the finite element formulation, and Eq. (34), (35),



the excitation and emission sensitivities at  $w^{th}$  node with respect to parameter  $p = \mu_{axf}$  can be expressed as (similar to Eq.(49)-(51) of [27])

$$\delta \underline{\Phi}_x^{(w)} = -\underline{\psi}_{xx}^{(w)T} \mathbf{F}\left(\Phi_x, \frac{\partial D_x}{\partial \mu_{axf}}, \frac{\partial k_x}{\partial \mu_{axf}}\right) \delta \underline{\mu}_{axf} \equiv \mathcal{L}_{xx}(\underline{\psi}_{xx}^{(w)}) \delta \underline{\mu}_{axf} \quad (37)$$

and

$$\begin{aligned} \delta \underline{\Phi}_m^{(w)} = & -\underline{\psi}_{xm}^{(w)T} \mathbf{F}\left(\Phi_x, \frac{\partial D_x}{\partial \mu_{axf}}, \frac{\partial k_x}{\partial \mu_{axf}}\right) \delta \underline{\mu}_{axf} - \underline{\psi}_{mm}^{(w)T} \mathbf{F}\left(\Phi_m, \frac{\partial D_m}{\partial \mu_{axf}}, \frac{\partial k_m}{\partial \mu_{axf}}\right) \delta \underline{\mu}_{axf} \\ & + \underline{\psi}_{mm}^{(w)T} \mathbf{U}\left(\Phi_x, \frac{\partial \beta}{\partial \mu_{axf}}\right) \delta \underline{\mu}_{axf} \equiv \mathcal{L}_{xm}(\underline{\psi}_{xm}^{(w)}) \delta \underline{\mu}_{axf} + \mathcal{L}_{mm}(\underline{\psi}_{mm}^{(w)}) \delta \underline{\mu}_{axf} \end{aligned} \quad (38)$$

$\mathbf{F}\left(\Phi_q, \frac{\partial D_q}{\partial \mu_{axf}}, \frac{\partial k_q}{\partial \mu_{axf}}\right)$  and  $\mathbf{U}\left(\Phi_x, \frac{\partial \beta}{\partial \mu_{axf}}\right)$ , ( $q = x, m$ ) are the assembled form of elemental matrices computed in a nodal basis in our work as:

$$\begin{aligned} \mathcal{F}\left(\Phi_q, \frac{\partial D_q}{\partial \mu_{axf}}, \frac{\partial k_q}{\partial \mu_{axf}}\right) = & \int_{\Omega_e} (\nabla[\mathbf{N}])^T \nabla[\mathbf{N}] \tilde{\Phi}_q \{[\mathbf{N}] \odot (\tilde{\sigma}_{D_q})^T\} \\ & + \int_{\Omega_e} [\mathbf{N}]^T [\mathbf{N}] \tilde{\Phi}_q \{[\mathbf{N}] \odot (\tilde{\sigma}_{k_q})^T\} \end{aligned} \quad (39)$$

and

$$\mathcal{U}\left(\Phi_x, \frac{\partial \beta}{\partial \mu_{axf}}\right) = \int_{\Omega_e} [\mathbf{N}]^T [\mathbf{N}] \tilde{\Phi}_x \{[\mathbf{N}] \odot (\tilde{\sigma}_\beta)^T\} \quad (40)$$

respectively, where  $\tilde{\sigma}_\beta = \phi[1 \ 1 \ 1]^T$ ,  $\tilde{\sigma}_{k_x} = [1 \ 1 \ 1]$  and  $\tilde{\sigma}_{k_m} = \gamma[1 \ 1 \ 1]^T$ , and  $\tilde{\sigma}_{D_x} = -1./[3(\tilde{k}_x + \tilde{\mu}'_{sx}).^2]$  and  $\tilde{\sigma}_{D_m} = -\gamma./[3(\tilde{k}_m + \tilde{\mu}'_{sm}).^2]$ , where  $\tilde{k}_{(x/m)}$ ,  $\tilde{\mu}_{s(x/m)}$  denote the vector of nodal values of corresponding parameters in element  $e$ , “./” denotes component-wise division, and “ $(\cdot)^2$ ” denotes component-wise squaring of the quantity in parentheses.

## References

1. L. V. Wang and H.-I. Wu, *Biomedical Optics: Principles and Imaging*, 1st ed. (Wiley-Interscience, U.S.A., 2007).
2. B. Cox, S. Arridge, and P. Beard, “Gradient-based quantitative photoacoustic image reconstruction for molecular imaging,” in *Photons Plus Ultrasound: Imaging and Sensing 2007: The Eighth Conference on Biomedical Thermoacoustics, Optoacoustics, and Acousto-optics*, vol. 6437 (International Society for Optics and Photonics, 2007), p. 64371T.
3. B. T. Cox, S. R. Arridge, and P. C. Beard, “Estimating chromophore distributions from multiwavelength photoacoustic images,” *JOSA A* **26**, 443–455 (2009).
4. G. Bal and K. Ren, “Multi-source quantitative photoacoustic tomography in a diffusive regime,” *Inverse Probl.* **27**, 075003 (2011).
5. H. Gao, H. Zhao, and S. Osher, “Bregman methods in quantitative photoacoustic tomography,” *Cam Rep.* **10**, 42 (2010).
6. H. Gao, S. Osher, and H. Zhao, “Quantitative photoacoustic tomography,” in *Mathematical Modeling in Biomedical Imaging II*, (Springer, 2012), pp. 131–158.
7. T. Saratoon, T. Tarvainen, B. Cox, and S. Arridge, “A gradient-based method for quantitative photoacoustic tomography using the radiative transfer equation,” *Inverse Probl.* **29**, 075006 (2013).
8. R. Hochuli, S. Powell, S. Arridge, and B. Cox, “Quantitative photoacoustic tomography using forward and adjoint monte carlo models of radiance,” *J. biomedical optics* **21**, 126004 (2016).

9. J. Buchmann, B. A. Kaplan, S. Powell, S. Prohaska, and J. Laufer, "Three-dimensional quantitative photoacoustic tomography using an adjoint radiance monte carlo model and gradient descent," *J. biomedical optics* **24**, 066001 (2019).
10. H. Gao, J. Feng, and L. Song, "Limited-view multi-source quantitative photoacoustic tomography," *Inverse Probl.* **31**, 065004 (2015).
11. M. Haltmeier, L. Neumann, and S. Rabanser, "Single-stage reconstruction algorithm for quantitative photoacoustic tomography," *Inverse Probl.* **31**, 065005 (2015).
12. S. Schoeder, M. Kronbichler, and W. Wall, "Photoacoustic image reconstruction: material detection and acoustical heterogeneities," *Inverse Probl.* **33**, 055010 (2017).
13. S. Rabanser, L. Neumann, and M. Haltmeier, "Stochastic proximal gradient algorithms for multi-source quantitative photoacoustic tomography," *Entropy* **20**, 121 (2018).
14. Z. Yuan, Q. Wang, and H. Jiang, "Reconstruction of optical absorption coefficient maps of heterogeneous media by photoacoustic tomography coupled with diffusion equation based regularized newton method," *Opt. express* **15**, 18076–18081 (2007).
15. Z. Yuan and H. Jiang, "Quantitative photoacoustic tomography," *Philos. Transactions Royal Soc. A: Math. Phys. Eng. Sci.* **367**, 3043–3054 (2009).
16. T. Tervainen, B. T. Cox, J. Kaipio, and S. R. Arridge, "Reconstructing absorption and scattering distributions in quantitative photoacoustic tomography," *Inverse Probl.* **28**, 084009 (2012).
17. Z. Yuan and H. Jiang, "A calibration-free, one-step method for quantitative photoacoustic tomography," *Med. physics* **39**, 6895–6899 (2012).
18. M. Venugopal, P. van Es, S. Manohar, D. Roy, and R. M. Vasu, "Quantitative photoacoustic tomography by stochastic search: direct recovery of the optical absorption field," *Opt. letters* **41**, 4202–4205 (2016).
19. A. Corlu, R. Choe, T. Durduran, M. A. Rosen, M. Schweiger, S. R. Arridge, M. D. Schnall, and A. G. Yodh, "Three-dimensional in vivo fluorescence diffuse optical tomography of breast cancer in humans," *Opt. Express* **15**, 6696–6716 (2007).
20. D. Yang, H. Wang, C. Sun, H. Zhao, K. Hu, W. Qin, R. Ma, F. Yin, X. Qin, Q. Zhang *et al.*, "Development of a high quantum yield dye for tumour imaging," *Chem. science* **8**, 6322–6326 (2017).
21. X. Cui, Q. Fan, S. Shi, W. Wen, D. Chen, H. Guo, Y. Xu, F. Gao, R. Nie, H. D. Ford *et al.*, "A novel near-infrared nanomaterial with high quantum efficiency and its applications in real time in vivo imaging," *Nanotechnology* **29**, 205705 (2018).
22. K. Ren and H. Zhao, "Quantitative fluorescence photoacoustic tomography," *SIAM J. on Imaging Sci.* **6**, 2404–2429 (2013).
23. K. Ren, R. Zhang, and Y. Zhong, "Inverse transport problems in quantitative pat for molecular imaging," *Inverse Probl.* **31**, 125012 (2015).
24. C. Wang and T. Zhou, "A hybrid reconstruction approach for absorption coefficient by fluorescence photoacoustic tomography," *Inverse Probl.* **35**, 025005 (2018).
25. P. K. Pandey, O. Gottam, N. Naik, P. Singh, and A. Pradhan, "One step quantitative fluorescence photoacoustic tomography," in *International Conference on Fibre Optics and Photonics*, (Optical Society of America, 2016), pp. P1A–24.
26. P. K. Pandey, O. Gottam, N. Naik, and A. Pradhan, "Comparative study of one-step and two-step quantitative fluorescence photoacoustic tomography," *Appl. optics* **58**, 3116–3127 (2019).
27. F. Fedele, J. Laible, and M. Eppstein, "Coupled complex adjoint sensitivities for frequency-domain fluorescence tomography: theory and vectorized implementation," *J. Comput. Phys.* **187**, 597–619 (2003).
28. Y. Sun, "Three-dimensional photoacoustic tomography and its application to detection of joint diseases in the hand," Ph.D. thesis, University of Florida (2010).
29. S. Bagchi, D. Roy, and R. M. Vasu, "Forward problem solution in photoacoustic tomography by discontinuous galerkin method," in *Bio-Optics: Design and Application*, (Optical Society of America, 2011), p. JTuA22.
30. Z. Yuan and H. Jiang, "Quantitative photoacoustic tomography: Recovery of optical absorption coefficient maps of heterogeneous media," *Appl. physics letters* **88**, 231101 (2006).
31. J. Nocedal and S. Wright, *Numerical optimization* (Springer Science & Business Media, 2006).
32. M. Schweiger, S. R. Arridge, and I. Nissilä, "Gauss–newton method for image reconstruction in diffuse optical tomography," *Phys. Medicine & Biol.* **50**, 2365 (2005).
33. A. Joshi, W. Bangerth, and E. M. Sevick-Muraca, "Adaptive finite element based tomography for fluorescence optical imaging in tissue," *Opt. Express* **12**, 5402–5417 (2004).
34. A. B. Thompson, "Development of a new optical imaging modality for detection of fluorescence-enhanced disease," Ph.D. thesis, Texas A & M University (2003).
35. A. Klose, "Optical tomography based on the equation of radiative transfer," Ph.D. thesis, Freie Universität Berlin (2002).